Ligand-Controlled Co-reduction *versus* Electroless Co-deposition: Synthesis of Nanodendrites with Spatially Defined Bimetallic Distributions

Nancy Ortiz, Rebecca G. Weiner, and Sara E. Skrabalak*

Department of Chemistry, Indiana University, 800 East Kirkwood Avenue, Bloomington, Indiana 47405, United States

ABSTRACT The predictable synthesis of bimetallic nanostructures *via* co-reduction of two metal precursors is challenging due to our limited understanding of precursor ligand effects. Here, the influence of different metal–ligand environments is systematically examined in the synthesis of Pd–Pt nanostructures as a model bimetallic system. Nanodendrites with different spatially defined Pd–Pt compositions are achieved, where the local ligand environments of metal precursors dictate if temporally separated co-reduction dominates to achieve core–shell nanostructures or whether electroless co-deposition proceeds to facilitate alloyed nanostructure formation. As the properties of bimetallic nanomaterials depend on crystal ordering and composition, chemical routes to structurally defined bimetallic nanomaterials are critically needed. The approaches reported here should be applicable to other bimetallic compositions given the established reactivity of coordination complexes available for use as precursors.

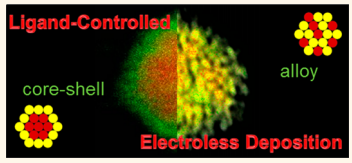

KEYWORDS: alloy · core–shell · palladium · platinum · nanoparticles · shape control

Interest in bimetallic nanostructures with core–shell, alloyed, or intermetallic distributions is growing on account of their applications in catalysis, where crystal ordering and composition can dramatically affect activity and selectivity.[1–7] For example, platinum and palladium are useful catalysts in many industrial processes,[8–11] and mixing the two metals in compositionally defined nanostructures can enhance performance. In fact, bimetallic Pd–Pt nanodendrites are often better catalysts for the electro-oxidation of ethanol, methanol, and formic acid compared to monometallic analogues.[12–15] However, achieving such bimetallic structures in a predictable manner by co-reduction of two metal precursors is challenging due to poor understanding of the chemical transformations that lead to nanostructures from metal precursors.[16–19] Here, we investigate the possibility of manipulating co-reduction in a model Pd–Pt system through selection of specific metal–ligand interactions in order to achieve bimetallic nanostructures with different spatially defined compositions (*e.g.*, alloy *versus* core–shell). Significantly, the local ligand environments of the metal precursors dictate whether or not electroless co-deposition can be achieved for alloy formation; otherwise, temporally separated co-reduction is evident, with core–shell architectures prevalent.

There are numerous reports of Pd–Pt dendritic structures, but to our knowledge, a comprehensive investigation on how the local ligand environments of metal precursors influence the bimetallic distribution in nanostructures achieved *via* co-reduction has not been undertaken. Yet from coordination chemistry, the local ligand environments of metal complexes are known to determine the thermodynamic and kinetic stability of precursors.[20] Thus, scenarios can be imagined in which the selection of precursors with different local ligand environments could give rise to nanostructures with different bimetallic spatial distributions *via* co-reduction (*e.g.*, temporally separated reduction toward core–shell structures or true co-reduction toward alloyed structures). Of course, this perspective assumes that diffusion or surface-to-ligand effects do not influence the bimetallic distribution after nanostructure formation.[21] Pd–Pt is an appropriate system for this study as the

* Address correspondence to sskrabal@indiana.edu.

Received for review September 17, 2014 and accepted December 5, 2014.

Published online December 09, 2014
10.1021/nn5052822

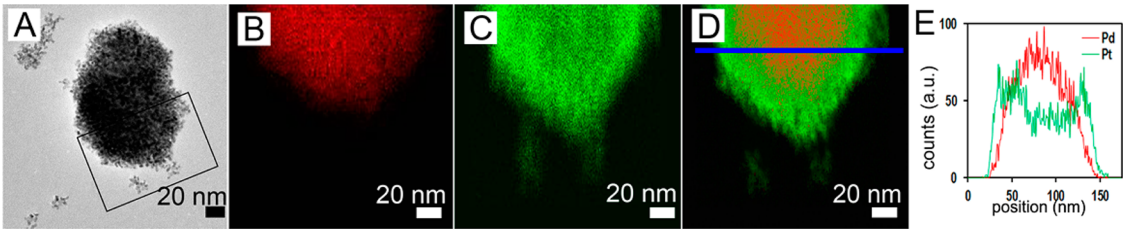

Figure 1. (A) TEM image of a Pd−Pt core−shell dendritic bundle with selected area used for STEM/EDX analysis. Elemental mapping of selected area denotes the presence of (B) Pd (red), (C) Pt (green), (D) combined Pd and Pt. In (E), an EDX line scan corresponding to the blue line in (D).

surface segregation energies of these metals within the other as a host are minimal compared to other bimetallic compositions, minimizing the contribution of diffusion to bimetallic distribution.[22,23]

We recently reported the formation of monometallic nanodendrites and single-crystalline nanoparticles through the manipulation of local ligand environments of Pd and Pt precursors.[24] Without a strongly coordinating ligand (*e.g.*, in oleylamine only), nanodendrites formed from common Pd and Pt precursors.[24] The insight gained from that study informs the selection of precursors for our model bimetallic system in which the formation of Pd−Pt nanostructures with different bimetallic distributions is facilitated by the minimal lattice mismatch (0.77%) between Pd and Pt.[25] Interestingly, nanodendrites with different spatially distributed bimetallic compositions are selectively formed. These structures are achieved by exploiting three metal−ligand precursor systems: (i) $Pd(acac)_2$ and $Pt(acac)_2$ in oleylamine only, (ii) $Pd(acac)_2$ and $Pt(hfac)_2$ in oleylamine only, and (iii) $Pd(acac)_2$ and H_2PtCl_6 in oleylamine only. Oleylamine serves as both the solvent and reducing agent. This selection minimizes the possibility for other components than ligand environment to contribute to nanostructure development, with amine-assisted reduction facilitating product formation.[26] The first two systems were selected to test the hypothesis that nanostructures with different bimetallic distributions can be achieved through manipulation of the reduction profiles of metal precursors *via* their local ligand environments. The last system serves as a model for electroless co-deposition catalyzed by a nanoparticle surface.

RESULTS AND DISCUSSION

In the first study, $Pd(acac)_2$ and $Pt(acac)_2$ were dissolved in oleylamine at a 1:1 mol ratio and heated at 160 °C (see Methods for experimental details). This temperature was selected because our previous study of these precursors individually in oleylamine found that while the reduction of $Pd(acac)_2$ is facile at lower temperatures, $Pt(acac)_2$ requires heating at a minimum of 160 °C to produce product in a reasonable time.[24] This finding is consistent with the greater stability of Pt complexes relative to Pd complexes.[20] Thus, we anticipated that the greater stability of $Pt(acac)_2$ compared to $Pd(acac)_2$ would provide ample difference in reduction rates to facilitate Pd and Pt metal segregation for core−shell Pd−Pt nanostructure formation. Indeed, pairing these metal precursors leads to nanodendrites with a core−shell distribution of Pd−Pt (Figure 1). The dendritic bundles form rapidly at 160 °C (Figure S1, Supporting Information), with the bimetallic composition confirmed by energy dispersive X-ray spectroscopy (EDX, Figure S2, Supporting Information). Elemental mapping by scanning transmission electron microscopy (STEM) coupled with EDX confirms the distribution of Pd and Pt within the nanodendritic bundles. From this analysis, Pd (red) is localized in the core and Pt (green) in the shell, with little mixing of the two as evident by the line scan analysis (Figures 1D,E). The formation of segregated Pd and Pt domains can be attributed to the greater stability of $Pt(acac)_2$ compared to $Pd(acac)_2$.

Dendritic structures can develop *via* overgrowth, etching, aggregation, or seed-mediated methods coupled with aggregation.[27] Our previous analysis of $Pd(acac)_2$ and $Pt(acac)_2$ reduction individually in oleylamine found that monometallic nanodendrites form and that these structures arise on account of aggregation-based growth.[24] Likewise, characterization of these Pd−Pt nanodendrites by TEM supports the aggregation-based growth pathway, although overgrowth from the dendritic structures likely occurs as well.[28] From Figure 2, adjacent regions within a dendritic bundle (region C of Figure 2A) or smaller nanodendrite (region B of Figure 2A) have different crystal orientations, as evident from FFT analysis (Figure 2B) or measurements of lattice spacings (Figure 2C). In addition, smaller dendritic structures are present in the sample. Such structural analysis is consistent with aggregation-based growth, where misorientation at particle interfaces is common after subparticle collision and gives rise to polycrystalline nanostructures.[13] Evidently, oleylamine is insufficient to stabilize the individual crystallites that form in solution. STEM/EDX analysis of the smaller dendritic structures supports the idea of temporally separated reduction of Pd and Pt precursors as these structures are nearly Pt-only in composition (Figure 2D).

In our previous study of monometallic Pd and Pt nanodendrite formation, the greater stability of $Pt(acac)_2$ relative to $Pd(acac)_2$ was evident by the dif-

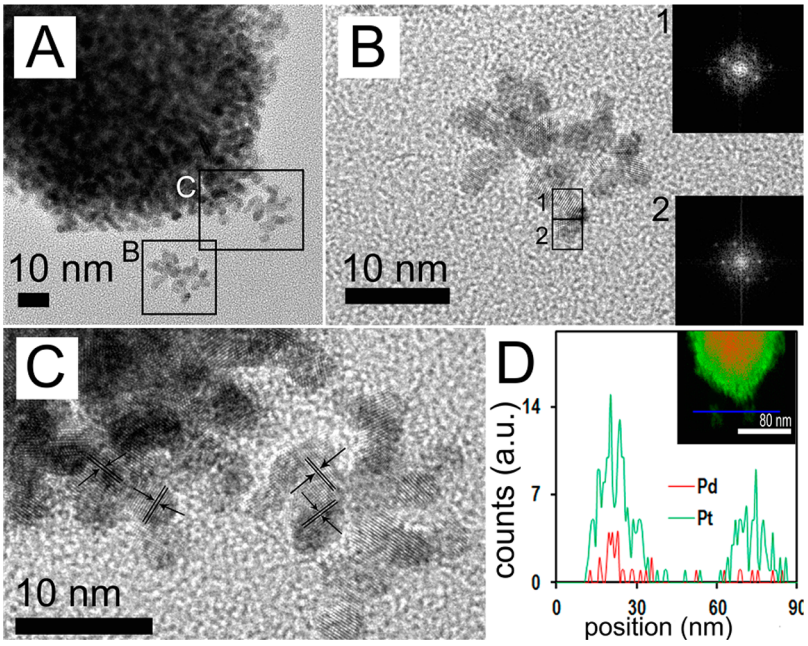

Figure 2. (A) TEM image of a Pd−Pt core−shell dendritic bundle with selected area used for higher magnification TEM analysis. (B) Higher magnification as denoted in (A), with the FFT (insets) of selected areas. (C) Higher magnification as denoted in (A), with different lattice directions of adjacent crystallites denoted. (D) EDX line scan profile of smaller nanodendrites (inset).

ferent temperatures required for product formation.[24] However, a direct comparison of metal generation at the same temperature was not made. Thus, the reduction processes of these precursors were studied individually in oleylamine at 160 °C. As expected, heating $Pd(acac)_2$ yields Pd nanodendrites within 5 min, which grow into larger bundle-like structures by 1 h (Figure S3, Supporting Information). However, the same experiment with $Pt(acac)_2$ yielded smaller particles, with very little product being isolated in the initial heating period (Figure S4, Supporting Information). Bundle-like structures were not observed within the time frame of the experiment. Thus, the combination of the facile reduction of $Pd(acac)_2$ in oleylamine paired with the more stable $Pt(acac)_2$ is an appropriate synthetic environment to favor formation of Pd−Pt core−shell nanodendrites. Likewise, pairing $Pd(hfac)_2$ and $Pt(hfac)_2$ at a 1:1 mol ratio for co-reduction in oleylamine only also generated core−shell Pd−Pt structures at equivalent reaction conditions (Figure S5, Supporting Information). This observation, too, can be attributed to the greater stability of Pt complexes compared to analogous Pd complexes.[20] Given the general trend in stability of Pd and Pt complexes, the selection of two metal precursors with the same metal−ligand environments to achieve core−shell structures emerges a general guideline. However, as discussed later, this concept only holds if other routes to nanostructure formation (*e.g.*, electroless deposition) are suppressed.

Second, precursor combinations where the local ligand environments of the Pt and Pd precursors are different were examined to test the hypothesis of whether or not the bimetallic distribution could be manipulated by matching reduction profiles to achieve bimetallic nanostructures with greater Pd−Pt mixing. With Pt complexes being overall more stable than their Pd analogs, $Pt(hfac)_2$ was paired with $Pd(acac)_2$ at a 1:1 mol ratio and heated to 160 °C. $Pt(hfac)_2$ was selected on account of the better leaving group properties of the $hfac^-$ ligands compared to the $acac^-$ ligands and our previous work, which verified more rapid growth of metal nanostructures from metal precursors with $hfac^-$ ligands.[29] Surprisingly, co-reduction of this precursor combination again generated nanostructures with a Pd−Pt core−shell architecture (Figure 3), although the Pt signal from STEM−EDX line scan analysis had to be multiplied 3× to explicitly reveal this spatial distribution (Figure 3E). Thus, Pd and Pt may be mixed more at the interface between Pd and Pt domains, but overall the reduction of $Pt(hfac)_2$ is still temporally separated compared to $Pd(acac)_2$, inhibiting alloy formation. This finding highlights the challenges in achieving bimetallic nanostructures predictably through co-reduction methods as selection of precursors guided by local ligand environment alone may be insufficient to manipulate the bimetallic spatial distributions. However, greater diversity of structures may be possible in systems where product formation proceeds *via* decomposition only (*e.g.*, $M_x^0L_y$) or when the reducing agent need not coordinate to the metal center to facilitate reduction (*e.g.*, selection of precursors with ligands capable of reduction themselves).

As these ligand-controlled co-reduction efforts did not manipulate the bimetallic distribution, new synthetic

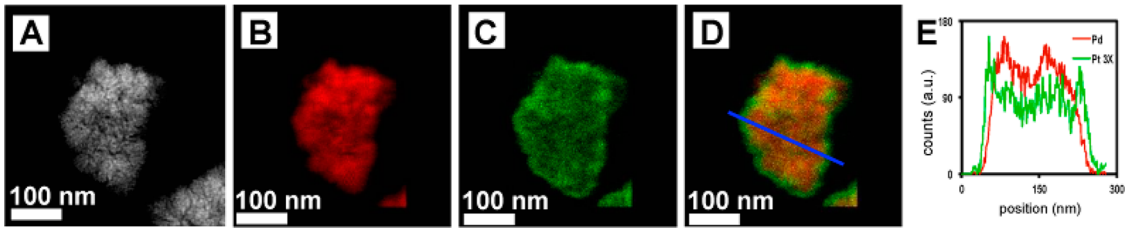

Figure 3. (A) STEM image of Pd−Pt core−shell nanodendrites 6 h after co-reducing $Pt(hfac)_2$ with $Pd(acac)_2$ in oleylamine at 160 °C. Elemental mapping by STEM-EDX denotes the presence of (B) Pd (red), (C) Pt (green), (D) combined Pd and Pt. (E) EDX line scan profile corresponding to blue line in (D), with 3× enhanced Pt signal to demonstrate the core−shell feature of the dendritic bundle.

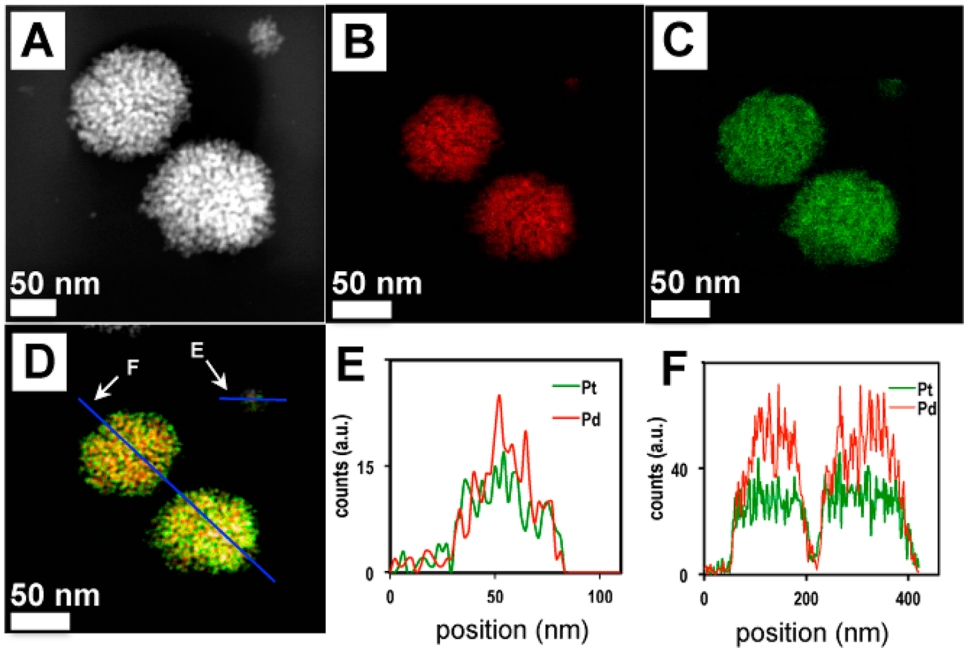

Figure 4. (A) STEM image of Pd−Pt alloy nanodendrites 6 h after co-reducing $Pd(acac)_2$ with H_2PtCl_6 in oleylamine at 160 °C. Elemental mapping by STEM−EDX denotes the presence of (B) Pd (red), (C) Pt (green), and (D) combined Pd and Pt. Line scan profiles of (E) a small dendrite and (F) larger dendritic bundles, corresponding to the blue lines in (D).

systems were envisioned. In particular, we were inspired by the rich history of electroless deposition as a route to bimetallic films[30−32] and hypothesized that a similar mechanism could facilitate alloy formation in colloidal systems. Electroless deposition broadly describes all processes of metal deposition without an external electrical current; however, it is more commonly used to describe catalyzed processes by which metallic ions M^{z+} are reduced to metal M *via* a reducing agent, with the overall process being catalyzed by the surface to which metal M is being deposited onto.[33] Typically, this process is used for film deposition onto substrates; however, the same chemical processes can occur at the surfaces of nanoparticles and is most commonly applied for core−shell nanoparticle formation.[34−36] As we demonstrate here, this surface catalyzed process can be exploited to co-reduce two metal precursors at nanoparticle surfaces, leading to bimetallic deposition and the formation of nanostructures with a mixed Pd−Pt distribution rather than core−shell architecture.

As is evident from the system containing $Pd(acac)_2$ and $Pt(acac)_2$, the $acac^-$ ligands protect the Pt precursor from the surfaces of the generated Pd nanodendrites and electroless deposition as little metal mixing is present in the final structure even though Pd can catalyze Pt deposition from Pt(II) precursors.[36] To realize electroless deposition, a new Pt source is required that is both stable in solution but easily reduced once at a Pd nanoparticle surface. These requirements are met with H_2PtCl_6 as a Pt(IV) source to Pt metal. Pt(IV) precursors are commonly used in electroless deposition techniques on account of their stability and need of a surface for nucleation, and such a mechanism has been cited with the generation of Pt−Pd/C structures, although no study of ligand effects was undertaken.[36−38] Here, when H_2PtCl_6 is heated in oleylamine at 160 °C, no product is produced, and no color changes are observed to indicate reduction of Pt(IV). However, when $Pd(acac)_2$ and H_2PtCl_6 are co-reduced in oleylamine at 160 °C, dendritic structures are produced and EDX analysis indicates the incorporation of Pt (Figures S6 and S7, Supporting Information). Elemental mapping by STEM/EDX shows that Pd and Pt are intimately mixed and not of a core−shell distribution (Figure 4).

TABLE 1. Pt:Pd Mole Ratio Determined by SEM–EDX of Core-Shell and Mixed Nanodendrites as a Function of Synthesis Time: 30 min and 1, 3, and 6 h

time	30 min	1 h	3 h	6 h
Pt:Pd core–shell	NA	0.05:1	1.4:1	1.1:1
Pt:Pd mixed	NA	0.5:1	0.5:1	0.27:1

Such mixing is characteristic of alloy formation; however, XRD cannot be used in Pd–Pt systems to confirm composition as Pd and Pt have overlaying patterns (PDF cards 00-005-0681 and 00-004-0802).

As the selected H_2PtCl_6 precursor was the only experimental modification, the observed Pd–Pt mixed phase suggests the necessity for a Pd seed to facilitate reduction of H_2PtCl_6, which in this case is achieved *in situ* by the reduction of $Pd(acac)_2$ at 160 °C. The need for a Pd surface was tested by injecting Pd seeds into a solution of H_2PtCl_6 in oleylamine at 160 °C. In the absence of Pd seeds, no color changes indicative of H_2PtCl_6 reduction are observed, and no product can be isolated. However, with injection of Pd seeds into the hot solution of H_2PtCl_6, nanostructures with a bimetallic composition are obtained (Figure S8, Supporting Information). From this control experiment, we conclude that deposition of Pt requires a Pd surface to catalyze the reduction of the Pt(IV) precursor. This electroless deposition process, however, exploits the surfaces of nanoparticles rather than an underlying substrate, as typically employed to deposit a film, and Pd continues to deposit during the process from the reduction of $Pd(acac)_2$. Finally, this mechanism is supported by comparing changes in the Pt:Pd ratio in the mixed Pd–Pt nanodendrites to the core–shell Pd–Pt nanodendrites as a function of synthesis time. The Pt:Pd ratios were obtained by SEM-EDX, with results summarized in Table 1. No product could be obtained at 30 min from the start of heating, which is consistent with the ramp time to reach 160 °C taking ~25 min. Notably, a dramatic difference between the two samples exists at 1 h of heating; very little Pt is present in the core–shell sample in comparison to the mixed system. This observation is consistent with the reduction of the Pt precursor being catalyzed in the mixed nanodendrite system but ligand-controlled in the core–shell system. By 3 h, the relative amount of Pt increases dramatically in the synthesis of core–shell nanodendrites, consistent with the slow reduction of the Pt precursor. By 6 h, the relative amount of Pt decreases in both samples, with the core–shell system yielding samples with a nearly 1:1 ratio, consistent with the starting precursor ratio. In contrast, the mixed system is enriched with Pd, highlighting that the composition of the catalyzing surface is likely to influence the degree to which the Pt precursor is reduced.

Often changes in chemical mechanism are accompanied by changes in nanostructure morphology. However, the dendritic morphology is maintained even with surface-catalyzed deposition. This finding is consistent with the aggregation-based mechanism that accounts for dendrite formation in which oleylamine is insufficient to provide full colloidal stability. Shown in Figure 4D is STEM/EDX analysis of two larger dendritic bundles along with a smaller, still detatched, dendrite; all have spatially mixed Pd–Pt compositions. Line scans for the small dendrite and bundles are in Figures 4E and F, respectively. Therefore, the larger bundles arise from aggregation of the smaller Pd–Pt dendrites, which themselves form through aggregation of smaller primary particles with a mixed Pd–Pt distribution. This composition is facilitated by electroless deposition on Pd generated *in situ*. As surface-catalyzed Pt deposition proceeds, additional $Pd(acac)_2$ is also reduced, facilitating the co-deposition of Pd and Pt onto the growing nanostructures. This finding highlights the complexity of nanomaterial syntheses, in which precursor selection alone cannot be condensed simply to its local ligand environment. Here, a surface-catalyzed process provides access to a different bimetallic distribution, where the reactivity of H_2PtCl_6 is modified with the presence of Pd but the reactivity of $Pt(acac)_2$ is not apparently influenced.

Given the broad use of electroless deposition methods in film preparation, exploiting this process with colloids as the catalyzing surface could provide access to a diversity of bimetallic nanostructures. The utility of this method was further demonstrated by varying the Pd–Pt mole ratio of the precursors in co-reduction from 2:1, 1:1, to 1:2. Figures S9–S11 (Supporting Information) contain characterization by EM, including elemental mapping by STEM-EDX of individual dendritic bundles. At low Pt concentration, no core–shell architecture is evident from the line scan (Figure S9E, Supporting Information) although the overall map (Figures S9B–D, Supporting Information) is mostly red, indicating a predominance of Pd (~80 mol % Pd of total metal content by EDX analysis). This characterization is consistent with the electroless deposition pathway to product. Likewise, no core–shell architecture is evident from the line scan of the sample prepared at 1:1 (Figures 4 and S10, Supporting Information). As expected, the amount of Pd in the final structure decreases from ~80 mol % to ~50 mol % by EDX analysis. Finally, at high Pt concentration, the mole % Pd decreases substantially to ~25%. This change is accompanied by a change in bimetallic distribution as well, with a Pd-enriched center, a mixed Pd–Pt middle, and a Pt-enriched surface as revealed by the line scan (Figure S11E, Supporting Information).

Differences in bimetallic distribution can dramatically influence the performance of catalysts, making the core–shell (Figure 1) and mixed (Figure 4) Pd–Pt nanodendrites ideal platforms for studying the architectural effects of bimetallic nanostructures.

Unfortunately, effective removal of the capping oleylamine either by electrochemical cycling or acid treatment[39,40] could not be achieved, as was evident by substantial carbon contamination of samples during TEM imaging post-treatment. Thus, reliable measurements for model reactions could not be obtained by standard methods.

CONCLUSIONS

Although studies report the synthesis of metal nanodendrites and other structurally distinct metal nanostructures,[41] few provide a detailed understanding of the metal precursor selection as they relate to nanostructure architecture and bimetallic distribution. Here, the influence of metal–ligand interactions was investigated systematically in a model Pd–Pt system, where nanostructures with different spatially defined compositions (alloy *versus* core–shell) were achieved. Ultimately, understanding these processes is important to controlling the growth and assembly of nanomaterials with defined compositions, structures, and in turn, properties. This work provides groundwork for predictive nanostructure formation and a pathway to metal heterostructures of tunable compositions. Just like the molecular programming approach used to prepare metal chalcogenide nanomaterials with defined compositions,[42–44] these methods connect principles of coordination chemistry to nanostructure formation and provide a paradigm for the rational design of materials regardless of composition. Central to the successful execution of this approach is the future recognition of the multiple roles that ligands can adopt in a synthesis and the ways in which the local ligand environment of precursors and colloids can change throughout a synthesis.[16]

METHODS

Chemicals. $Pd(acac)_2$ (99%), $Pd(hfac)_2$ (99%), $Pt(hfac)_2$ (99.9%), and $H_2PtCl_6 \cdot 6H_2O$ (99.9%) were obtained and used as received from Strem Chemicals, Inc. Oleylamine (OLA, technical grade, 70%) and $Pt(acac)_2$ (99%) were purchased from Sigma-Aldrich.

Characterization. TEM was conducted with a JEOL JEM 1010 microscope operating at 80 kV equipped with a ROM CCD camera. High-resolution TEM images were acquired with a JEOL JEM 3500FS microscope using a 4k × 4k Gatan UltraScan 4000 CCD camera. All samples were redispersed in hexanes and drop-casted on Ted Pella copper grids with Formvar or carbon coating. The JEOL JEM 3200FS was interfaced with an Oxford INCA dispersive X-ray system for collection of EDX spectra. Large area EDX analysis was obtained with a FEI Quanta 600F Environmental scanning electron microscope operated at 30 kV and a spot size of 3 which was interfaced with an Oxford INCA detector for EDX spectra collection.

Synthesis of Core–Shell Pd–Pt Dendrites. $Pd(acac)_2$ (0.055 mmol) and $Pt(acac)_2$ (0.055 mmol) were co-dissolved in oleylamine (22 mL) to create a yellow solution. The solution was heated under continuous stirring from room temperature to 160 °C (ramp rate ca. 20 °C min^{-1}), over the course of which a color change was observed from pale yellow to dark black. Other core–shell compositions using either $Pd(hfac)_2$ with $Pt(hfac)_2$ or $Pd(acac)_2$ with $Pt(hfac)_2$ followed the same concentrations and experimental conditions.

Synthesis of Mixed Pd–Pt Dendrites. $Pd(acac)_2$ (0.055 mmol) and $H_2PtCl_6 \cdot 6H_2O$ (0.055 mmol) were co-dissolved in oleylamine (22 mL) to create a yellow solution. The solution was heated under continuous stirring from room temperature to 160 °C (ramp rate ca. 20 °C min^{-1}), over the course of which a color change was observed from pale yellow to dark black.

Control Experiment. $H_2PtCl_6 \cdot 6H_2O$ (0.055 mmol) in oleylamine (22 mL) was heated from room temperature to 160 °C (ramp rate ca. 20 °C min^{-1}). Then oleylamine-capped Pd particles were injected into the solution as seeds for Pt deposition. The Pd particles were prepared by heating $Pd(acac)_2$ in oleylamine for a short period of time in order to limit the formation of large dendritic structures.

Conflict of Interest: The authors declare no competing financial interest.

Supporting Information Available: additional characterization and results from control experiments. This material is available free of charge *via* the Internet at http://pubs.acs.org.

Acknowledgment. We thank the IU Nanoscale Characterization Facility for access to instrumentation. This work was supported by start-up funds from Indiana University and NSF Award CHE-1306853. S.E.S. is a Cottrell Scholar (Research Corporation), Sloan Research Fellow, and Camille Dreyfus Teacher–Scholar.

REFERENCES AND NOTES

1. Strasser, P. Dealloyed Core-Shell Fuel Cell Electrocatalysts. *Rev. Chem. Eng.* **2009**, *25*, 255–295.
2. Toshima, N.; Yonezawa, T. Bimetallic Nanoparticles - Novel Materials for Chemical and Physical Applications. *New J. Chem.* **1998**, *22*, 1179–1201.
3. Ferrando, R.; Jellinek, J.; Johnston, R. L. Nanoalloys: From Theory to Applications of Alloy Clusters and Nanoparticles. *Chem. Rev.* **2008**, *108*, 845–910.
4. Sankar, M.; Dimitratos, N.; Miedziak, P. J.; Wells, P. P.; Kiely, C. J.; Hutchings, G. J. Designing Bimetallic Catalysts for a Green and Sustainable Future. *Chem. Soc. Rev.* **2012**, *41*, 8099–8139.
5. Ataee-Esfahani, H.; Imura, M.; Yamauchi, Y. All-Metal Mesoporous Nanocolloids: Solution-Phase Synthesis of Core–Shell Pd@Pt Nanoparticles with a Designed Concave Surface. *Angew. Chem., Int. Ed.* **2013**, *52*, 13611–13615.
6. Ataee-Esfahani, H.; Liu, J.; Hu, M.; Miyamoto, N.; Tominaka, S.; Wu, K. C. W.; Yamauchi, Y. Mesoporous Metallic Cells: Design of Uniformly Sized Hollow Mesoporous Pt–Ru Particles with Tunable Shell Thicknesses. *Small* **2013**, *9*, 1047–1051.
7. Yamauchi, Y. Field-Induced alignment controls of one-dimensional mesochannels in mesoporous materials. *J. Ceram. Soc. Jpn.* **2013**, *121*, 831–840.
8. Roucoux, A.; Schulz, J.; Patin, H. Reduced Transition Metal Colloids: A Novel Family of Reusable Catalysts? *Chem. Rev.* **2002**, *102*, 3757–3778.
9. Wang, F.; Li, C. H.; Sun, L. D.; Xu, C. H.; Wang, J. F.; Yu, J. C.; Yan, C. H. Porous Single-Crystalline Palladium Nanoparticles with High Catalytic Activities. *Angew. Chem., Int. Ed.* **2012**, *51*, 4872–4876.
10. Chen, J.; Lim, B.; Lee, E. P.; Xia, Y. Shape-Controlled Synthesis of Platinum Nanocrystals for Catalytic and Electrocatalytic Applications. *Nano Today* **2009**, *4*, 81–95.
11. Astruc, D. Palladium Nanoparticles as Efficient Green Homogeneous and Heterogeneous Carbon-Carbon Coupling Precatalysts: A Unifying View. *Inorg. Chem.* **2007**, *46*, 1884–1894.
12. Wang, L.; Nemoto, Y.; Yamauchi, Y. Direct Synthesis of Spatially-Controlled Pt-on-Pd Bimetallic Nanodendrites with Superior Electrocatalytic Activity. *J. Am. Chem. Soc.* **2011**, *133*, 9674–9677.

13. Xia, Y.; Xiong, Y.; Lim, B.; Skrabalak, S. E. Shape-Controlled Synthesis of Metal Nanocrystals: Simple Chemistry Meets Complex Physics? *Angew. Chem., Int. Ed.* **2009**, *48*, 60–103.
14. Wang, L.; Yamauchi, Y. Facile Synthesis of Three-Dimensional Dendritic Platinum Nanoelectrocatalyst. *Chem. Mater.* **2009**, *21*, 3562–3569.
15. Watt, J.; Young, N.; Haigh, S.; Kirkland, A.; Tilley, R. D. Synthesis and Structural Characterization of Branched Palladium Nanostructures. *Adv. Mater.* **2009**, *21*, 2288–2293.
16. Ortiz, N.; Skrabalak, S. E. On the Dual Roles of Ligands in the Synthesis of Colloidal Metal Nanostructures. *Langmuir* **2014**, *30*, 6649–6659.
17. Zhou, S.; Jackson, G. S.; Eichhorn, B. AuPt Alloy Nanoparticles for CO-Tolerant Hydrogen Activation: Architectural Effects in Au-Pt Bimetallic Nanocatalysts. *Adv. Funct. Mater.* **2007**, *17*, 3099–3104.
18. Wang, Y.; Toshima, N. Preparation of Pd-Pt Bimetallic Colloids with Controllable Core/Shell Structures. *J. Phys. Chem. B* **1997**, *101*, 5301–5306.
19. Wu, J.; Gross, A.; Yang, H. Shape and Composition-Controlled Platinum Alloy Nanocrystals Using Carbon Monoxide as Reducing Agent. *Nano Lett.* **2011**, *11*, 798–802.
20. Cotton, F. A.; Wilkinson, G.; Murillo, C. A.; Bochmann, M. *Advanced Inorganic Chemistry*, 6th ed.; Wiley-Interscience: New York, 1999.
21. Schaak, R. E.; Sra, A. K.; Leonard, B. M.; Cable, R. E.; Bauer, J. C.; Han, Y. F.; Means, J.; Teizer, W.; Vasquez, Y.; Funck, E. S. Metallurgy in a Beaker: Nanoparticle Toolkit for the Rapid Low-temperature Solution Synthesis of Functional Multimetallic Solid-State Materials. *J. Am. Chem. Soc.* **2005**, *127*, 3506–3515.
22. Ma, Y.; Balbuena, P. B. Pt Surface Segregation in Bimetallic Pt_3M Alloys: A Density Functional Theory Study. *Surf. Sci.* **2008**, *602*, 107–113.
23. Nilekar, A. U.; Ruban, A. V.; Mavrikakis, M. Surface Segregation Energies in Low-index Open Surfaces of Bimetallic Transition Metal Alloys. *Surf. Sci.* **2009**, *603*, 91–96.
24. Ortiz, N.; Skrabalak, S. E. Manipulating Local Ligand Environments for the Controlled Nucleation of Metal Nanoparticles and their Assembly into Nanodendrites. *Angew. Chem., Int. Ed.* **2012**, *51*, 11757–11761.
25. Habas, S. E.; Lee, H.; Radmilovic, V.; Somorjai, G. A.; Yang, P. Shaping Binary Metal Nanocrystals through Epitaxial Seeded Growth. *Nat. Mater.* **2007**, *6*, 692–697.
26. Mourdikoudis, S.; Liz-Marzan, L. M. Oleylamine in Nanoparticle Synthesis. *Chem. Mater.* **2013**, *25*, 1465–1476.
27. Lim, B.; Xia, Y. Metal Nanocrystals with Highly Branched Morphologies. *Angew. Chem., Int. Ed.* **2011**, *50*, 76–85.
28. Cao, G. *Nanostructures and Nanomaterials*; Imperial College Press: London, 2004.
29. Siedle, A. R.; Pignolet, L. H. 4:1 Lewis Base Adducts of Palladium bis(hexafluoroacetylacetonate). The Structure of $(4\text{-}ClC_5H_4N)_4Pd(C_5HF_6O_2)_2$. *Inorg. Chem.* **1982**, *21*, 135–141.
30. Ohno, I. Electrochemistry of Electroless Plating. *Mater. Sci. Eng.* **1991**, *A146*, 33–49.
31. Djokic, S. S., Electroless Deposition of Metals and Alloys. In *Modern Aspects of Electrochemistry*; Conway, B. E., White, R. E., Eds.; Kluwer Academic/Plenum Publishers: Fort Saskatchewan, 2002; Vol. 35, p 51.
32. Kerr, C.; Barker, D.; Walsh, F. Electroless Deposition of Metals. *Trans. Inst. Met. Finish.* **2001**, *79*, 41–46.
33. Djokić, S., Electroless Deposition of Metals and Alloys. In *Modern Aspects of Electrochemistry*; Conway, B., White, R., Eds.; Springer: New York, 2002; Vol. 35, pp 51–133.
34. Beard, K. D.; Borrelli, D.; Cramer, A. M.; Blom, D.; Van Zee, J. W.; Monnier, J. R. Preparation and Structural Analysis of Carbon-Supported Co Core/Pt Shell Electrocatalysts Using Electroless Deposition Methods. *ACS Nano* **2009**, *3*, 2841–2853.
35. Beard, K. D.; Schaal, M. T.; Van Zee, J. W.; Monnier, J. R. Preparation of Highly Dispersed PEM Fuel Cell Catalysts using Electroless Deposition Methods. *Appl. Catal. B - Environ.* **2007**, *72*, 262–271.
36. Ohashi, M.; Beard, K. D.; Ma, S. G.; Blom, D. A.; St-Pierre, J.; Van Zee, J. W.; Monnier, J. R. Electrochemical and Structural Characterization of Carbon-supported Pt-Pd Bimetallic Electrocatalysts Prepared by Electroless Deposition. *Electrochim. Acta* **2010**, *55*, 7376–7384.
37. Rao, C. R. K.; Trivedi, D. C. Chemical and Electrochemical Depositions of Platinum Group Metals and Their Applications. *Coord. Chem. Rev.* **2005**, *249*, 613–631.
38. Cho, S. J.; Ouyang, J. Y. Attachment of Platinum Nanoparticles to Substrates by Coating and Polyol Reduction of A Platinum Precursor. *J. Phys. Chem. C* **2011**, *115*, 8519–8526.
39. Li, D.; Wang, C.; Tripkovic, D.; Sun, S.; Markovic, N. M.; Stamenkovic, V. R. Surfactant Removal for Colloidal Nanoparticles from Solution Synthesis: The Effect on Catalytic Performance. *ACS Catal.* **2012**, *2*, 1358–1362.
40. Mazumder, V.; Sun, S. Oleylamine-Mediated Synthesis of Pd Nanoparticles for Catalytic Formic Acid Oxidation. *J. Am. Chem. Soc.* **2009**, *131*, 4588–4589.
41. Lim, B.; Wang, J.; Camargo, P. H. C.; Cobley, C. M.; Kim, M. J.; Xia, Y. Twin-Induced Growth of Palladium–Platinum Alloy Nanocrystals. *Angew. Chem., Int. Ed.* **2009**, *48*, 6304–6308.
42. Vela, J. Molecular Chemistry to the Fore: New Insights into the Fascinating World of Photoactive Colloidal Semiconductor Nanocrystals. *J. Phys. Chem. Lett.* **2013**, *4*, 653–668.
43. Ruberu, T. P. A.; Albright, H. R.; Callis, B.; Ward, B.; Cisneros, J.; Fan, H.-J.; Vela, J. Molecular Control of the Nanoscale: Effect of Phosphine-Chalcogenide Reactivity on CdS-CdSe Nanocrystal Composition and Morphology. *ACS Nano* **2012**, *6*, 5348–5359.
44. Guo, Y.; Alvarado, S. R.; Barclay, J. D.; Vela, J. Shape-Programmed Nanofabrication: Understanding the Reactivity of Dichalcogenide Precursors. *ACS Nano* **2013**, *7*, 3616–3626.